STM JOURNALS

Journal of NanoScience, NanoEngineering & Applications
ISSN: 2231-1777(online), ISSN: 2321-5194(print)
Volume 5, Issue 3
www.stmjournals.com

Application of Atomic Force Microscopy for the Study of Lithium-Ion Batteries

Shu-Wei Wang[1,2], Shi-Qiang Huang[2], Yan Jin[2,3], Deyu Wang[2]*, Cai Shen[2]*

[1]School of Materials Science and Engineering, Shanghai University, Shanghai, China
[2]Ningbo Institute of Materials Technology & Engineering, Chinese Academy of Sciences, China
[3]Nano Science and Technology Institute, University of Science and Technology of China, Suzhou

Abstract

Development of advanced Lithium Ion Batteries (LIBs) represents a fast growing field of science and technology. However, many fundamental problems remained unresolved due to lack of understanding of surface/interface phenomenon of LIB on nanometer scale. Here, we review recent applications of atomic force microscopy to study three key aspects of lithium ion batteries namely solid electrolyte interface, ion transportation and dendrite growth. In situ AFM is an ideal tool for the study of solid electrolyte interface and lithium deposition because of its real time and non-invasive. It is highly expected significant advances will be made in the coming years on this research area.

Keywords: *Atomic force microscopy, lithium ions, imaging, batteries, microscopic*

****Author for Correspondence*** E-mail: shencai@nimte.ac.cn, wangdy@nimte.ac.cn

INTRODUCTION

Scanning probe microscopy (SPM) includes a series of microscopic techniques in which a physical tip is moved by piezoelectric actuator to characterize sample surface. Some of the most commonly used SPM include scanning tunneling microscopy (STM) and atomic force microscopy (AFM). STM measures electronic current between the substrate and tip. It is one of the first few instruments used to reveal structure of material surface atomic scale. However, STM can only be used to measure surface properties of materials with conducting and semiconducting properties [1–9]. AFM was invented with the aim to expand SPM ability to measure surface properties of insulators, semiconductors and conductors. Figure 1 shows schematic drawing of AFM. The primary imaging modes of AFM are contact and tapping mode.

In contact mode, the value of the repulsive force between tip and sample remains unchanged during scanning. Meanwhile, in tapping mode, constant oscillation amplitude is maintained to obtain constant tip-sample interaction. A "phase" image is obtained by recording the phase differences between drive signal and cantilever response. Tapping mode is non-invasive and offers higher lateral resolution [10].

Lithium-ion batteries (LIBs) are one of the most efficient energy storage systems. Figure 2 shows the schematic view of a LIB. LIBs have been widely used in portable electronics because of their high specific energy, high energy density and good cycle life. However, new generation of LIBs with better performance are required for large scale applications in hybrid and electric vehicles [11, 12]. In order to design better batteries, efficient characterization methods are required to obtain accurate information on interfacial chemistry and morphology of batteries. Some of the most commonly used interfacial characterization techniques include X-ray photoelectron spectroscopy (XPS), Fourier transform infrared spectroscopy (FTIR), Raman spectroscopy (FT-Raman), scanning electron microscopy (SEM) and transmission electron microscopy (TEM).

However, aforementioned methods are invasive techniques which might destroyed the samples due to exposure to high energy beams. On the other hand, in situ AFM can provide real time changes on the sample surface with minimal destruction [13–20]. For

example, AFM has been used to image dendrite growth and corrosion of current collectors which lead to postulation of the mechanism of aforementioned phenomenon [21]. In this paper, we briefly reviewed the application of AFM for the study of LIBs including use of AFM to study solid electrolyte interface (SEI) on anode and cathode, ion transportation in LIB and Li deposition process during charge/discharge.

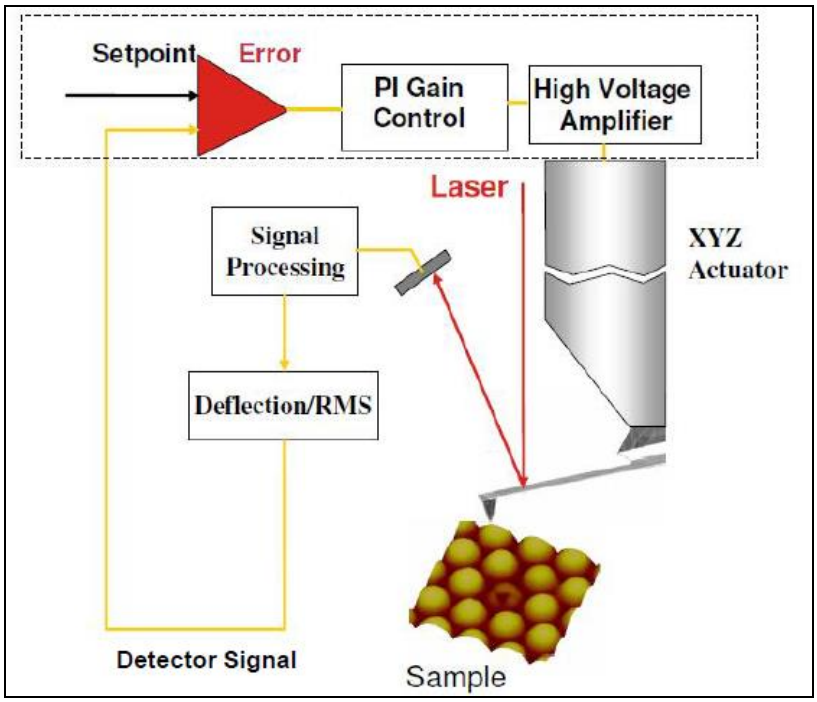

Fig. 1: *Schematic Drawing of AFM.*

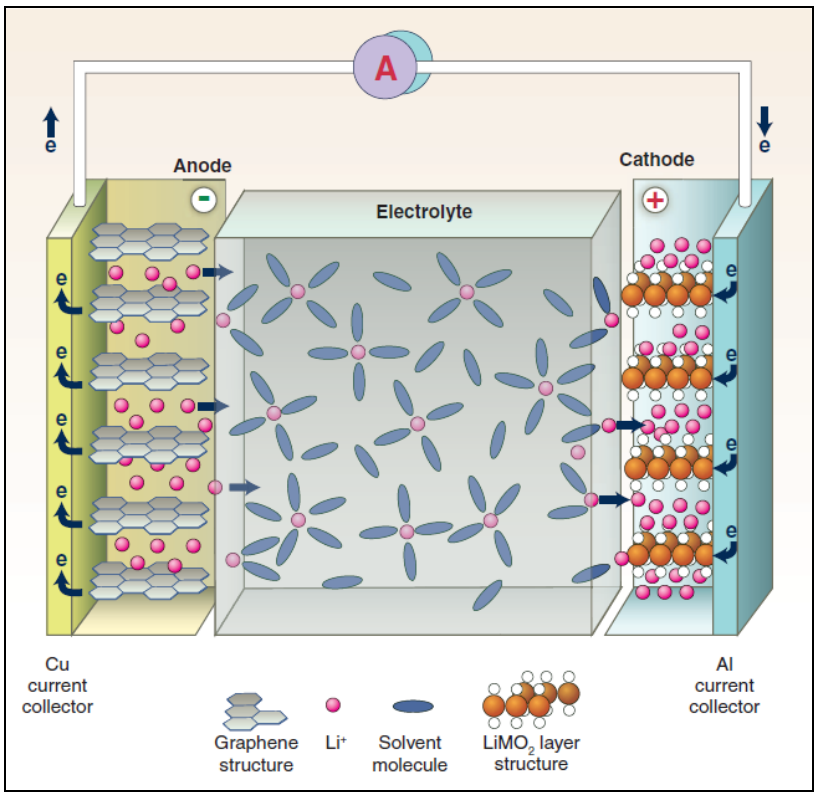

Fig. 2: *Schematic View of a LIB.*

SOLID ELECTROLYTE INTERFACE (SEI)

SEI is essentially a passivation film formed on anode/electrolyte or cathode/electrolyte interphase during initial stage of discharge/charge. SEI film is a Li^+ conductor and electric insulator. It plays a critical role in LIB, but remain the least understood part in LIBs [22, 23]. SEI affects Li^+ intercalation and dictates the kinetics of LIB reactions [24–30]. It is difficult to understand SEI layer because of the elusive manner of its formation, delicate chemical nature, heterogeneity in morphology and lack of reliable in situ characterization tools [9]. AFM is an in situ tool capable of providing structural and topographical information of interfacial structure which allows us to gain direct insight into the complicated processes occurring at electrolyte/electrode interphase [9, 31]. It can also provide information on mechanical properties of SEI such as mechanical strength and the thickness [32, 33].

Anode

Two Distinct Layers of SEI on Anode

SEI layer is generally accepted to compose of two distinct layers. Shin *et al.* characterized the in homogeneity of SEI using a combination of AFM/XPS analysis [34]. After 25 cycles in 1 M $LiPF_6$ dissolved in a mixture of ethylene carbonate (EC) and dimethyl carbonate (DMC) (1:1, vol. ration), the average elastic modulus is about 3.8 ± 5.6 GPa. After scratching the outer portion of the SEI using AFM probe, the average elastic modulus increased to 8.3 ± 11.5 GPa. This indicated that inner portion of the SEI layer have higher elastic modulus as compared to outer portion of the SEI layer. Using XPS and atomistic calculations, Shin *et al.* found that inner and outer parts of the SEI layer was composed of dense inorganic components such as LiF, Li_2CO_3 and porous polymers such as PEO, LiMC, LiEC, Li_2EDC, respectively [34].

Thickness of SEI on Anode

The two distinct layers of SEI have different thickness, chemical composition and rigidity. Domi and co-workers estimated the thickness of SEI layer using AFM [13]. HOPG electrode was cycled in 1 M $LiClO_4$ dissolved in a mixture of ethylene carbonate (EC) and dimethyl carbonate (DMC) (1:1, vol. ratio) at a scanning rate of 0.5 mV/s between 3.0 and 0.55 V. They scrapped off the layers by scanning the surface repeatedly in contact mode. The thickness of the precipitate layer on the HOPG edge plane is 56 ± 8 nm, and the one on the basal plane is 47 ± 4 nm after the first cyclic voltammetry (CV). Following the second CV, the thickness of the layer on the edge plane and basal plane is 66 ± 3 nm and 77 ± 5 nm, respectively. After the first cycle, SEI layer on the edge plane is thicker than that on the basal plane because of high activity of the edge plane as compared to the basal plane. From the first to second cycle, the SEI on the basal plane was thicker than the SEI on the edge plane. This indicated that passivation layer formed on edge plane might be more effective than that on the basal plane and could suppress further decomposition in the following cycles. In addition, composition of SEI layers formed on edge plane was found to be different from that on basal plane due to different degree of passivation. In another study, Domi *et al*. estimated the thickness of SEI layers formed with vinylene carbonate (VC) and vinyl ethylene carbonate (VEC) additives in 1 M $LiClO_4$/PC electrolyte [35]. They concluded that SEI layer formed in PC based electrolyte with VC and VEC additives was more superior than that formed in EC based solvent. Cresce *et al.* used in situ AFM to quantitatively characterize the SEI layer [32]. Interphase formed on HOPG was found to be heterogeneous. They utilized force-displacement spectroscopy to evaluate the SEI thickness. Figure 3 shows the force-displacement approach curve recorded on SEI layer in which repulsive interactions between the probe and sample surface caused cantilever to deflect nearly 0.25 μm. The probe used in this study displaced only the upper layer portion of SEI and thus estimated only the thickness of the upper layer portion of SEI. Thickness of the upper layer interphase ranged from 10 to 480 nm (102 ± 119 nm, N=15). Force-displacement spectroscopy enabled an accurate and statistical estimate of the thickness of the soft upper layer. Complementary XPS analysis of the two different SEI layers confirmed the organic nature of the soft upper layer and the inorganic nature of the hard under layer.

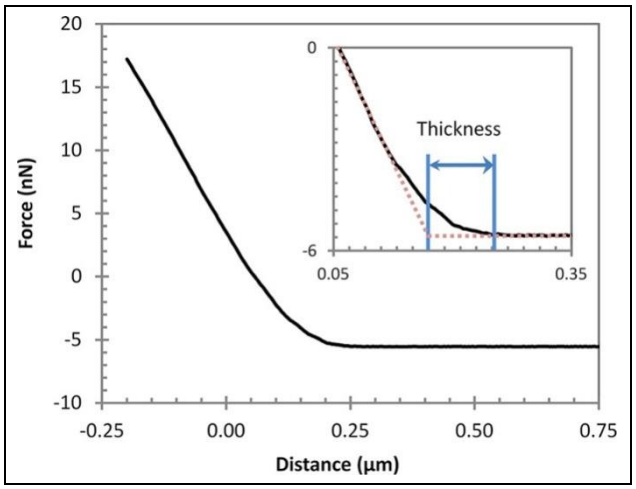

Fig. 3: *Force-Distance Approach Curve of AFM Probe toward SEI.*
Inset: *Magnification showing the estimated thickness. Same axes as the larger graph.*

Dotted lines shows the probe behavior on an SEI-free HOPG surface in electrolyte at OCV, before SEI formation, i.e., behavior on a hard surface.

Effects of Anode Volume Expansion on SEI Layer

LiF is the main component of SEI layer. Its inorganic nature cannot bear large volumetric changes of anodes [22, 36]. Martin *et al.* investigated the surface change during cycling of CuO thin film in 1 M $LiPF_6$ dissolved in a mixture of ethylene carbonate (EC), propylene carbonate (PC) and dimethyl carbonate (DMC) (1:1:3, vol. ratio) with 2 wt% of V C using AFM [37]. The first CV was performed between 0.8 and 3.5 V at a scanning rate of 5 µV/s. During the first discharge, the variation of the surface morphology is caused by formation of SEI and conversion reaction by insertion of Li^+, which induced volume expansion. During the first charge, large nodules disappeared and cracks were observed at the end of the first charge. The cracks disappeared during the next discharge and the film again expanded to fill the crack due to the Li^+ insertion. They concluded that cracks were induced by repetitively volume expansion/contraction of conversion materials. Lucas *et al.* investigated the SEI formation on tin foil electrode in an EC based electrolyte using in situ AFM [38]. The electrolyte used was 1 M $LiPF_6$ dissolved in a mixture of EC and DEC (1:2, weight ratio). They found homogeneous surface film consisted of small separate grains that fused into large agglomerates indicating that EC-based electrolyte were unable to produce efficient SEI layer. Large volumetric changes of Sn upon lithium insertion/deinsertion further induced the instability of SEI layer, which led to continuous regeneration of fresh tin surface and electrolyte decomposition.

In Situ Observation of SEI Layer in Various Electrolytes

$LiPF_6$ is the salt commonly used in majority of commercial LIBs. We recently investigated the morphological and compositional differences of SEI layer formed from EC and FEC-based electrolytes on HOPG electrode [34]. The electrolytes used were 1 M $LiPF_6$ in EC (or FEC)/DMC solution (1:1, vol. ratio). SEI layer started to grow after voltage swept down to ~0.8 V for EC-based electrolyte and ~1.0 V for FEC-based electrolyte. SEI layer formed at a slow scanning rate of 0.5 mV/s was dense and compact. The SEI layer formed was stable with no damage found even under maximum force scanned by AFM in contact mode. Our result confirmed previously reported findings on SEI layer started to form at higher potential for FEC-based electrolytes because of introduction of a F group into an ester which reduced the energy barrier [9]. Complemented with XPS for chemical characterization, our results showed that LiF was the main component for SEI formed from FEC/DMC electrolyte which might be the possible reason why SEI layer formed in FEC/DMC electrolyte was stable against scratching by AFM tip (Figure 4).

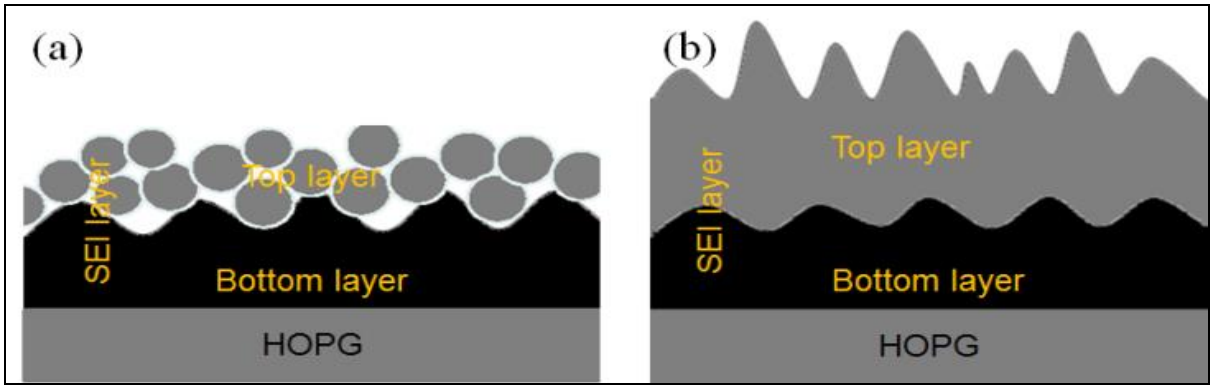

Fig. 4: *Model for the SEI Layers Formed from (a) $LiPF_6$/EC/DMC Electrolyte and (b) $LiPF_6$/FEC/DMC Electrolyte.*

One should note $LiPF_6$ was far from being prefect, because of its chemical and thermal instability. Many efforts have been made to develop new lithium salts. $TFSI^-$ anion might participates in SEI formation at a larger extent than PF_6^-. It also offers higher solubility (up to 5 M) and ion conductivity (up to 8 mS/cm) than $LiPF_6$ based electrolytes. Moreover, it is thermally stable up to 180 °C [39, 40]. AFM has been used to study the formation of SEI layer with new lithium salts. Liu *et al*. reported that electrolyte concentration affects the interfacial reactions between graphite and DMSO-based electrolytes [41]. They provided direct evidence for SEI layers formation and morphological evolution of HOPG in electrolytes with various concentrations using in situ AFM. An inhomogeneous layer was found to form at the step edges at potential lower than 0.7 V. In 1.0 M LiTFSI/DMSO electrolyte, the step edges were covered by passivation at the potentials above 1.5 V. This passivation was unable to prevent the constant co-intercalation of Li+. In 2.62 M LiTFSI/DMSO electrolyte, thin layers were formed at step edges at potential of around 0.5 V which prevented further co-intercalation or decomposition of the electrolyte. These results confirmed that high salt concentration was effective in assisting SEI layers formation and preventing the co-intercalation of Li+ solvation and structural deterioration of the HOPG surface. The passive layers formed at the step edge allow effective reversible Li+insertion/deinsertion at the graphite electrode (Figure 5).

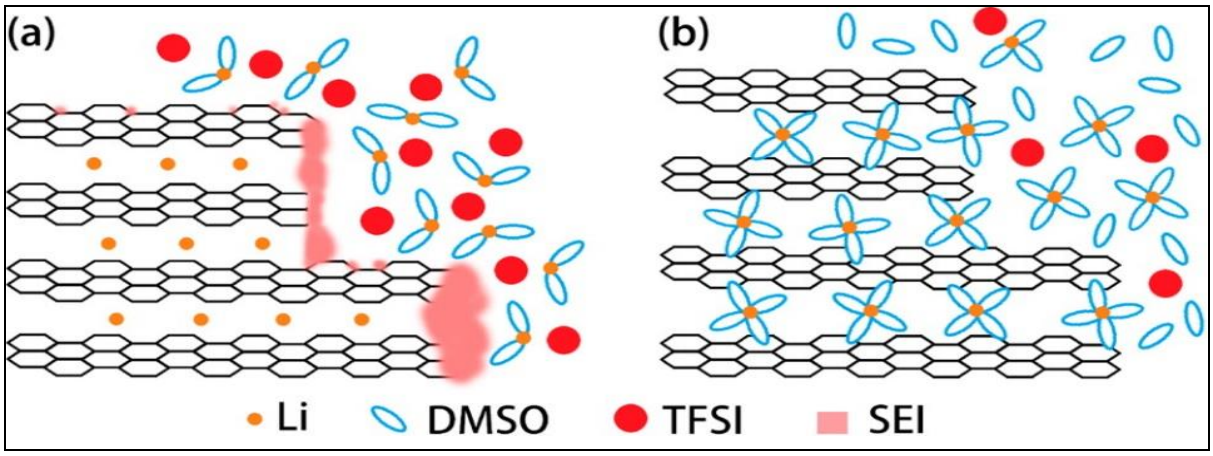

Fig. 5: *Model Diagram of (a) Highly Concentrated DMSO-based Electrolyte and (b) Diute DMSO-based Electrolyte Interface Reactions of Graphite Electrode.*

Temperature-Induced Morphological Changes in SEI

Edström *et al.* showed that AFM can be used to monitor temperature-induced morphological changes of SEI layer. SEI layer was found to cover the entire HOPG surface after single CV [16]. No significant changes can be observed between ambient temperature and 40°C. The blisters became clearly visible and larger with increasing temperature. Small blisters were clearly observed on the surface at 50°C which continue to grow into larger blisters as temperature increased to 70°C. Through XPS analysis, a thick carbon- and oxygen-containing layer was obtained at elevated temperatures. Similar findings were reported by Mogi *et al.* who found faster film formation and thicker SEI layer at 80°C as compared to that at room temperature [42]. In combination with CV measurements, it can be concluded that electrolyte decomposition was accelerated at elevated temperature.

Cathode

To date, limited effort has been put into understanding of the interphase on cathodes. Its role as passivation layer on cathodes was doubted because of its coverage on cathode surfaces was often found to be incomplete. The complicated species on cathode made it difficult to discern the decomposition product from electrolyte. The native surface on cathode exhibited superior capacity retention and rate capability [43 –54]. Many cathode materials have low electronic conductivity, which is difficult for SEM study. However, AFM can easily observe the surface morphology [55]. Vanadium oxides (V_2O_5) have been investigated a lot because of its high capacity. Cohen and Aurbach used AFM to observe the passivation layers formation on V_2O_5 cathode [56]. The V_2O_5 thin film electrodes were cycled in 1 M $LiPF_6$ or $LiClO_4$ dissolved in PC solution between 3.6 V–3.0 V. During intercalation, they noticed that nano size round shaped grains appeared on the boundaries of the V_2O_5 particles which remained stable after deintercalation. However, no significant changes in morphology were observed in experiment conducted in LiClO4/PC solution. They concluded that LiPF6 electrolyte has a major impact on the morphology of V2O5 cathode, which might be due to passivation layer formed by the reaction of LiPF6 on cathode. Mrowiecka et al. investigated morphology changes of V2O5 films after different cycles of CVs by AFM [57]. The pristine material prepared by thermal oxidation of metallic vanadium has a non-homogeneous composition with a gradual evolution from V to V2O5. The electrode was cycled between 3.8–2.8 V in 1 M LiClO4/PC solution. After 700 cycles, AFM images showed the process of grain exfoliation. After 2450 cycles, observation of the inner layer of the oxide film revealed formation of pits due to grain exfoliation. After 4500 cycles, the exfoliation process proceeded inwards towards the oxide film, and the surface appeared amorphous with small grains having no well-defined crystalline shape. The thin film were stripped away by rinsing to reveal the vanadium metal substrate. AFM images also showed the formation of pits ran along the grain boundaries. Complemented with XPS for chemical characterization, it was found that lithium carbonate and lithium-alkyl carbonate species were the main components of the SEI layer.

Fleutot *et al.* investigated the formation and dissolution process of SEI layer on V_2O_5 during Galvano static cycles using AFM [58]. The experiment was performed in 1 M $LiPF_6$/PC/EC/DM/DEC (4:2:9:5, vol. ratio) between 3.7–1.5 V. The topographic image acquired at the end of the charge exhibited thin films of V_2O_5 covered with a residual deposit. These species appeared increasingly on the surface during the next cycles. The main morphology modifications appear between the 10th and 30th charge (Figure 6). In agreement to the morphology modifications, XPS analysis revealed that main chemical modification also appeared between the 10th and 30th cycle. Changes in the morphology and chemical properties of SEI were the reason for capacity loss in the following cycles.

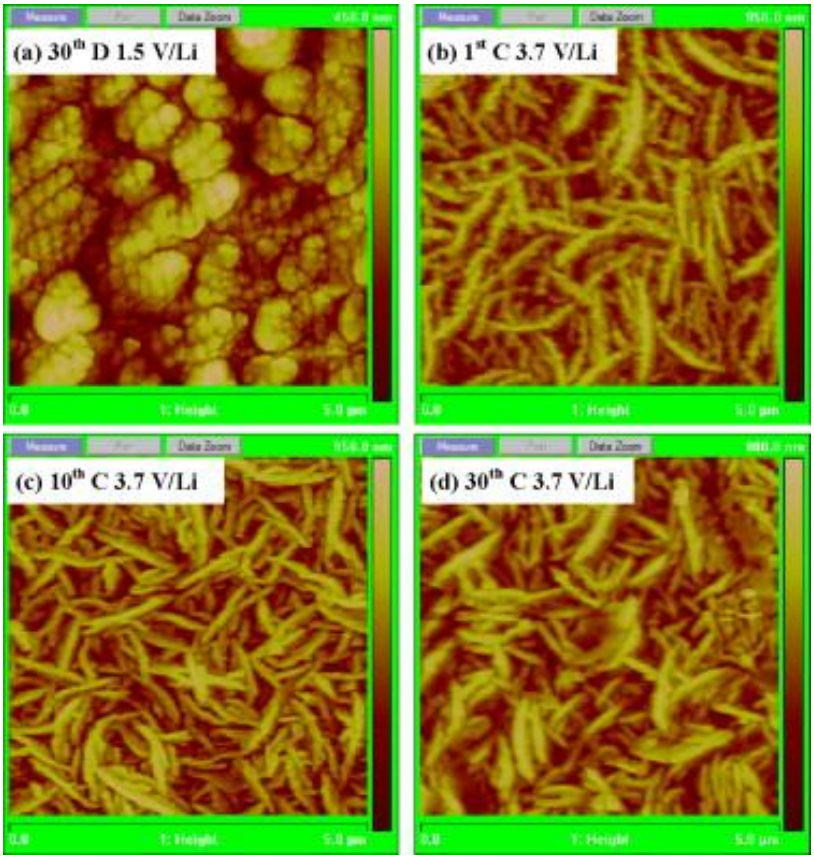

Fig. 6: *AFM Image of V_2O_5 (a) at the End of the 30th Discharge (1.5 V/Li); (b) at the End of the 1st Charge (3.7 V/Li); (c) at the End of the 10th Charge (3.7 V/Li); (d) at the End of the 30th Charge (3.7 V/Li).*

Doi *et al.* studied the changes in surface morphology of $LiMn_2O_4$ thin film cathode in 1 M $LiPF_6$/PC after repeated CVs or storage at elevated temperatures using in situ AFM [59]. No significant changes were observed after 90th cycles (3.5 V–4.3 V) at 25°C. However, changes in surface morphology can be observed at cycling temperature of 60°C. Particles covering the entire surface became smaller after the 30th cycles (3.5–4.3 V). Changes in morphology at 60°C were postulated to be closely related to capacity fading of the $LiMn_2O_4$ thin film. The grain size remained almost unchanged up to 24 h of storage at 50 and 100% depth of discharge. However, grains of $LiMn_2O_4$ clearly became smaller after storage at 75% depth of discharge for 4 h. Formation of small grains on the $LiMn_2O_4$ surface caused the loss of crystallinity, which accelerated the dissolution/precipitation reaction. They concluded that stability of $LiMn_2O_4$ is essential to obtain highly reversible charge/discharge reaction at 75% depth of discharge at elevated temperature. The host structure of electrode materials plays an important role in the performance and cycle life characteristics of LIB. Dong and co-workers investigated the surface morphology changes of $LiNi_{0.5}Mn_{1.5}O_4$ particle electrodes by in situ AFM [60]. The $LiNi_{0.5}Mn_{1.5}O_4$ electrode was cycled between 3.8–4.85 V. No significant changes in surface morphology was observed with the Li^+ de-intercalation until the potential exceeds 4.73 V. Particles deposited on the (111) surface can be attributed to the SEI layer formation at around 4.78 V. SEI layer remained stable with the decrease in potential (Figure 7). Unlike the (111) surface, no significant changes in surface morphology can be observed on the (100) surface. Thickness of the SEI layer was evaluated using contact mode. Thickness of the (111) surface was found to be about 4–5 nm. They concluded that the (111) surface formed a stable SEI layer and exhibited superior capacity retention and cycle life.

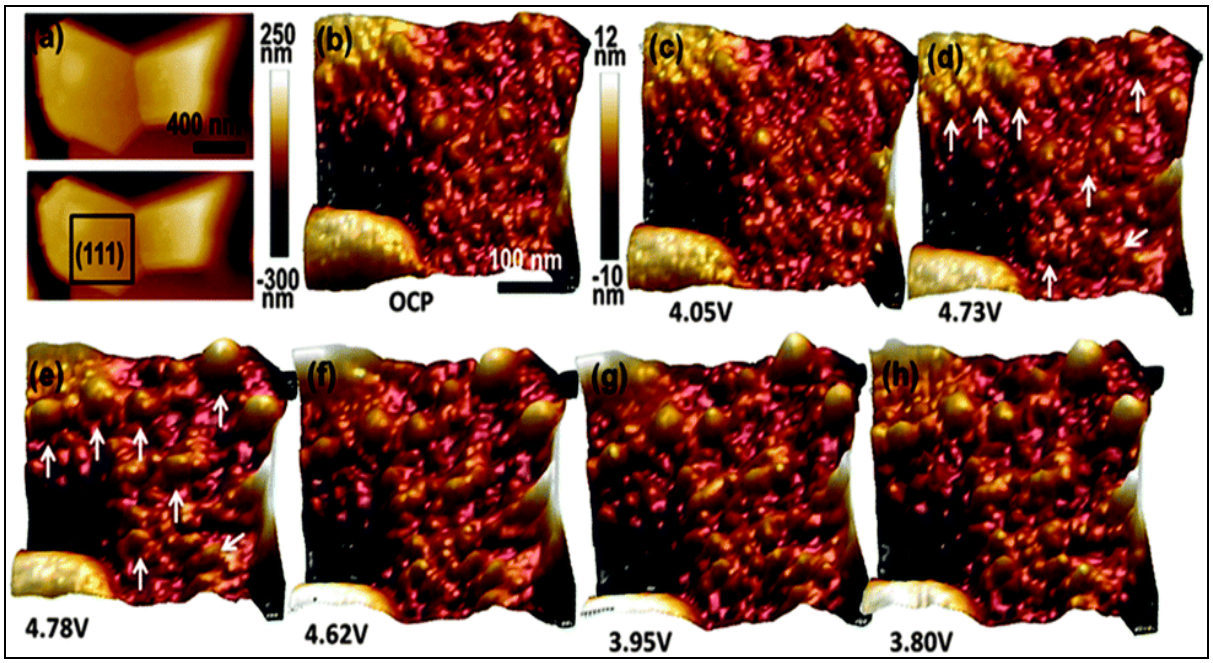

Fig. 7: *(a) Two-Dimensional AFM Images of $LiNi_{0.5}Mn_{1.5}O_4$ (111) and (100) Surfaces; (b–h) In situ AFM Three-Dimensional Images of the $LiNi_{0.5}Mn_{1.5}O_4$ (111) Surface during the First Charge–Discharge Cycle. The Area of the Image is 400×400 nm.*

Ion Transportation in Lithium Ion Batteries

Li-ions experience insertion/extraction processes between the anode and cathode materials during the charge/discharge processes. The irreversible transportation of Li-ions may lead to the impedance increase and capacity fading of batteries. Distinct metrics including a short ion and electron transport length and a large surface area are beneficial to improve Li-ions battery performances [61].

Hence, understanding of the mechanisms of the Li-ion transportation and the associated phenomenon is highly desired to develop new generation battery materials. In recent years, strain-based atomic force microscopy (s-AFM) have being used to study the ion transportation during the charge/discharge process [62]. Among the s-AFM techniques, electrochemical strain microscopy (ESM) and piezo-response force microscopy (PFM) have been demonstrated as reliable s-AFM modes for the probing of local Li-ion diffusion and related electrochemical activities [62–65].

ESM is different from PFM in the origins of the obtained signals. ESM has been used for exploring electrochemical strain resulting from ionic motion below AFM cantilever. Meanwhile, PFM has been used for studying piezoelectric properties and polarization states [63]. ESM is based on the application of high-frequency periodic electric bias through the conductive tip between anode and cathode. The bias induces localized change of volume and surface deformation resulting from Li-ion diffusion, migration and redistribution within the material. By measuring the amplitude of the surface oscillations or current-voltage characteristics, concentration changes of Li-ions during the charge/discharge processes can be obtained. Figure 8 shows the working principle of the AFM in which a biased atomic force microscopy tip is used to contact with an ionically conductive material.

The concentrated field at the tip induces ion redistribution, which in turn brings in the change of material strain and surface deformation. The latter is detected as vertical tip displacement [63, 66]. The major improvements of ESM over other current technologies were reflected by two points: (a) the resolution to probe nanometer-scale volumes and (b) imaging capability extended to a broad range of spectroscopic techniques. This technology has been used to study Li-ion transport in high storage density Si anode materials, TiO_2 anode, LiPON electrolyte and $LiNi_{1/3}Co_{1/3}Mn_{1/3}O_2$, $LiCoO_2$ cathode materials [64, 67, 68].

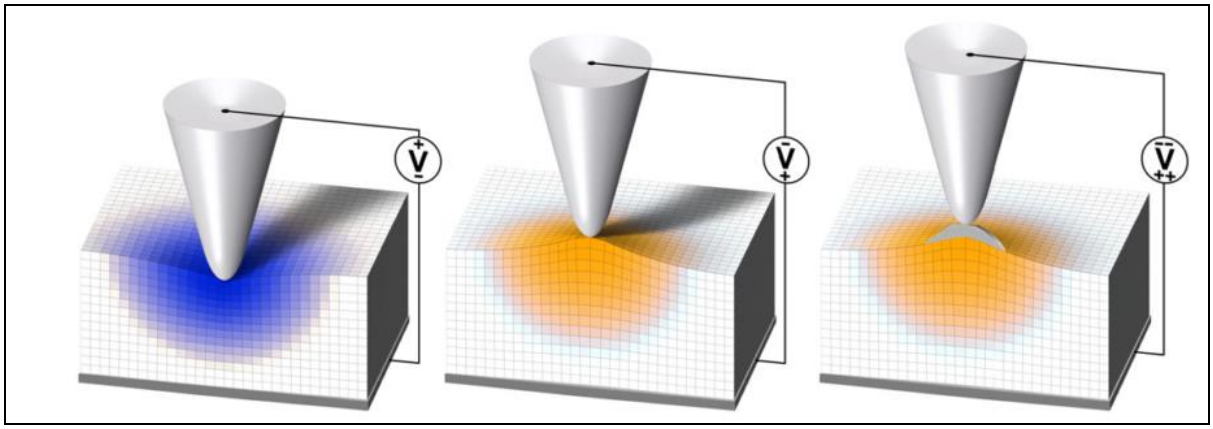

Fig. 8: *Working Principle of the ESM, a Biased AFM Tip is used to Contact with the Ionically Conductive Working Electrode. During Positive Bias Application, Li^+ is Depleted Under the Tip (Left Image), while at Negative Bias Polarity Li^+ is drawn toward the Tip (Middle Image). The Right Image shows the Li(s) Particle which forms when a Critical Negative Bias is Exceeded and Faradaic Charge Transfer takes Place.*

Li *et al.* observed electric current images of Li_xCoO_2 thin films using ESM and found that local conductance is closely associated with localized Li deficiency [69, 70]. They suggested that Li_xCoO_2 grain boundary area has a lower Li-ion diffusion energy barrier and higher Li-ion diffusion rate than grain interiors. Balke also studied $LiCoO_2$ using AFM to concentrate a periodic electric field into the cathode, triggering lithium ions to intercalate or de-intercalate, causing periodic changes in cathode volume and strain at the cathode [68]. The basic principle was shown in Figure 9. This strain was measured by the same AFM tip, producing a map of lithium intercalation and transport processes.

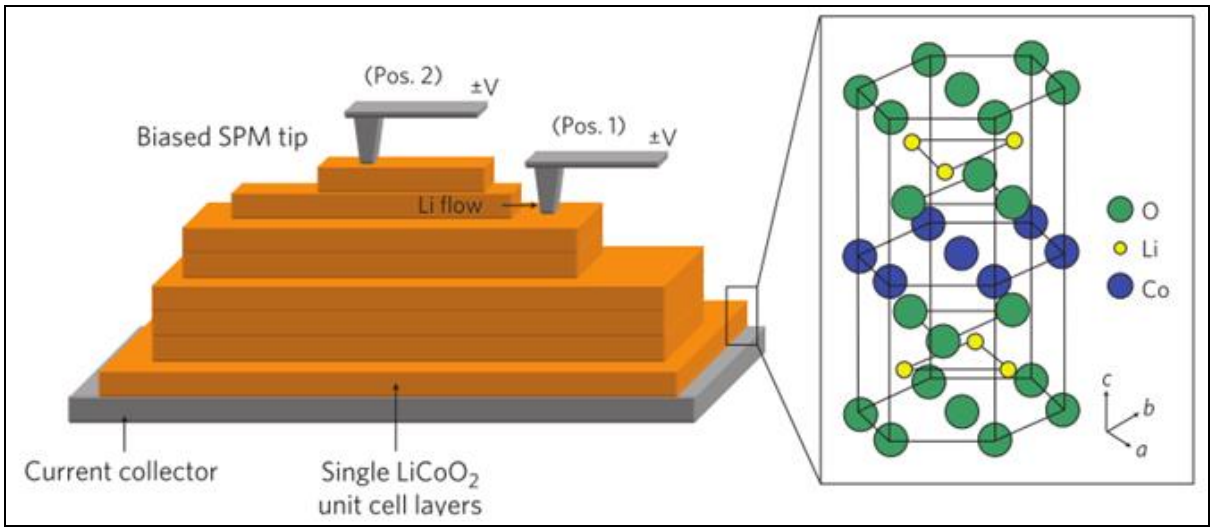

Fig. 9: *The Basic Principle of the Process. Schematic of a $LiCoO_2$ Grain, Consisting of Layers of Single Unit Cells, A biased SPM Tip Next to a Step (Position 1) will Induce a Flow of Lithium along the Lithium Layer. However, if the Tip is placed on a Basal Plane (Position 2), No Flow will be generated through the Close-Packed Oxygen Layers.*

Li Deposition Processes Studied by AFM

The theoretical specific capacity of lithium metal is 3860 mAh/g, and the negative electrochemical potential of lithium metal is –3.04 V(vs. standard hydrogen electrode), which made it a promising anode material for Li-based batteries [71]. Lithium batteries were firstly manufactured using lithium metal anode

and TiS_2 cathode in the late 1970s to early 1980s. Lithium metal reacted easily with electrolyte forming SEI on the surface because of its high reactivity. Nevertheless, such structure was not smooth enough causing lithium deposition during charge [72]. The inevitable mechanical deformation during Li plating/striping caused such weak SEI film to break and be repaired by reacting with more electrolyte. If the SEI film was not repaired at the breaking point with strong local flux of lithium ions deposition, Li dendrite will formed [73]. The formation of dendrite is very harmful to battery and pose severe safety concern for LIBs. Thus, it is essential to learn the process of Li deposition. AFM is a useful technique to study Li deposition processes. Aurbach and Cohen applied AFM for the study of Li deposition processes [74]. They discovered that the scanning of the tip did not change the morphology of target surface and the deposited Li in $LiPF_6$ solutions was more uniform than that in $LiClO_4$ solutions. They also suggested that the protective surface films formed in alkyl carbonated solutions were not flexible enough to accommodate the volume changes caused by Li deposition. Cracks appeared on films and became the preferred locations for Li deposition and finally Li dendrite was formed. Figure 10 showed the mechanism of Li electrodes during Li deposition [75].

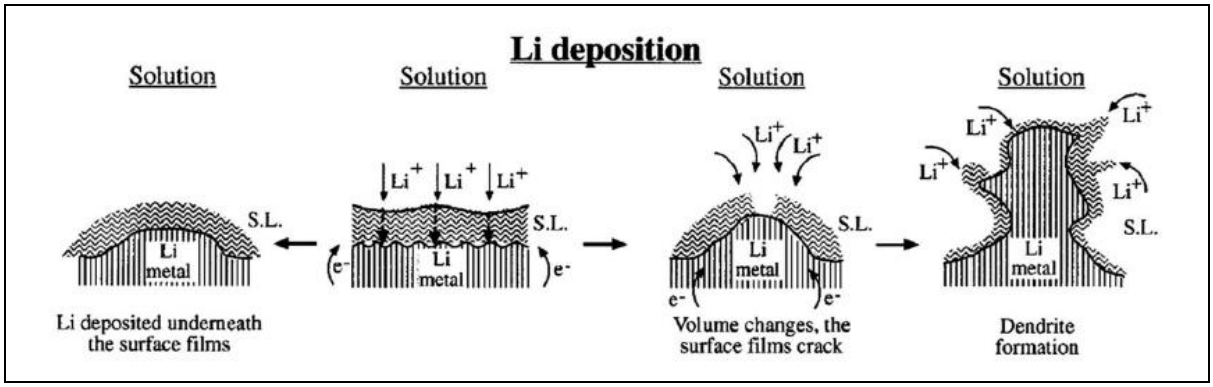

Fig. 10: *The Mechanism of Li Electrodes during Li Deposition.*

Zempachi and co-workers investigated the effect of temperature on lithium deposition on Ni substrate by AFM [76, 77]. In comparison with the surface film formed at room temperature and 40°C, surface films formed at 60 and 80°C were stable, smooth and homogeneous. Furthermore, lithium dendrite was suppressed by rapid self-repairability and increased surface diffusion of lithium atoms. Jeff Dahn and co-workers used in situ AFM to study the electrochemical reaction of lithium with tin [78].

Decomposition of electrolyte and formation of film were observed at 1.6 V. Through AFM study, they found the tower-like structure to be expanded when lithium was inserted. The tower-like structure contracted with removal of lithium. Sn tower did not get back to its initial state with removal of lithium. Figure 11 showed the change in morphology of Sn tower [78]. Such volume expansion of Sn was different from amorphous Si or amorphous Si-Sn.

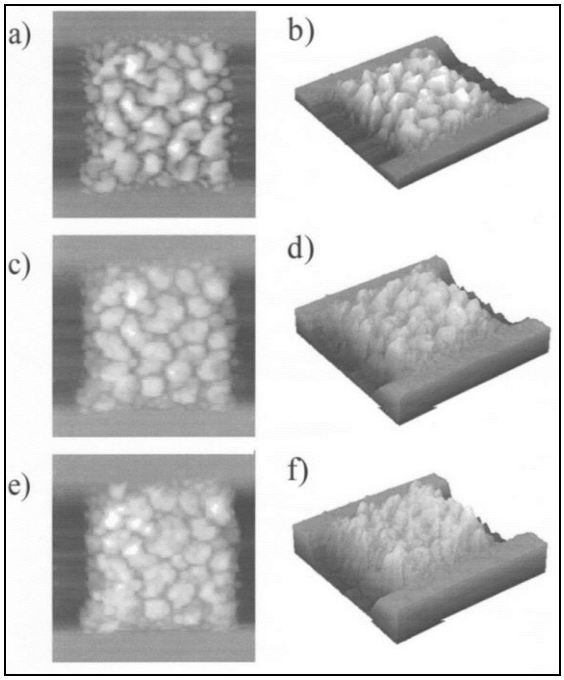

Fig. 11: *AFM Images of the Changes in Morphology of the Sn Tower. 2D and 3D Images of (a) and (b) Scan 000 (c) and (d) scan 225 and (e) and (f) scan 449.*

SUMMARY

AFM can be used in both in situ and ex situ for the study of surface morphology of electrodes. In this review, we mainly address the applications of AFM in the study of SEI layers, ion transportation, and lithium deposition process. Compared to conventional method to evaluate electrolytes, which are usually complex and tedious procedures, in situ electrochemical AFM combining with XPS could potentially serve as a fast diagnostic tool to evaluate the properties and quality of SEI layer formed on different electrodes from diverse electrolytes and additives. The development of advanced mode of AFM such as electrochemical strain microscopy makes the measurement of ion transportation in solid electrode possible. Dendrite formation poses a server threat for the safety of LIBs. The mechanism of the dendrite formation has been the hot topic in the past decade. However, no much process has been making due to the lack of reliable in situ techniques. In situ AFM is an ideal tool for the study of lithium deposition because of its real time and non-invasive. It is highly expected significant advances will be made in the coming years on this research area.

ACKNOWLEDGEMENT

We thank the National Natural Science Foundation of China (Grant No. 21303236). Cai thanks the financial support from the Youth Innovation Promotion Association, CAS and SRF for ROCS, SEM.

REFERENCES

1. Cebula I, Shen C, Buck M. *Angew Chem Int Edit*. 2010; 49: 6220–6223p.
2. Shen C, Buck M. *Beilstein J Nanotech*. 2014; 5: 258–267p.
3. Shen C, Cebula I, Brown C et al. *Chem Sci*. 2012; 3: 1858–1865p.
4. Shen C, Haryono M, Grohmann A et al. *Langmuir*. 2008; 24: 12883–12891p.
5. Cramer JR, Ning YX, Shen C et al. *Eur J Org Chem*. 2013; 2813–2822p.
6. Zhang J, Wang R, Yang XC, W et al. *Nano Lett*. 2012; 12: 2153–2157p.
7. Zheng JY, Zheng H, Wang R et al. *Phys Chem Chem Phys*. 2014; 16: 13229 –13238p.
8. Zhu J, Feng JK, Lu L et al. *J Power Sources*. 2012; 197: 224–230p.
9. Xu K. *Chemical Reviews*. 2014; 114: 11503–11618p.
10. Benitez R, Toca-Herrera JL. *Microscopy Research and Technique*. 2014; 77: 947–958p.
11. Bruce Dunn HK, Jean-Marie Tarascon. *Science*. 2011; 334: 928–935p.
12. Frederick BL, Wagner T, Mark F Mathias. *The Journal of Physical Chemistry Letters*. 2010; 1: 2204–2219p.
13. Domi Y, Ochida M, Tsubouchi S et al. *The Journal of Physical Chemistry C*. 2011; 115: 25484–25489p.
14. Deng X, Liu XR, Yan HJ et al. *Sci China Chem*. 2014; 57: 178–183p.
15. Demirocak DE, Bhushan B. *J Colloid Interf Sci*. 2014; 423: 151–157p.
16. Edstrom K, Herranen M. *J Electrochem Soc*. 2000; 147: 3628–3632p.
17. Lacey SD, Wan JY, Cresce AV et al. *Nano Lett*. 2015; 15: 1018–1024p.
18. Liu XR, Wang D, Wan LJ. *Sci Bull*. 2015; 60: 839–849p.
19. Wang LX, Deng D, Lev LC et al. *J Power Sources*. 2014; 265: 140–148p.
20. Wen R, Hong M, Byon HR. *J Am Chem Soc*. 2013; 135: 10870–10876p.
21. Younesi R, Veith GM, Johansson P et al. *Energy & Environmental Science*. 2015; 8: 1905–1922p.
22. AgubraVA, Fergus JW. *J Power Sources*. 2014; 268: 153–162p.
23. Winter M. *Z. Phys. Chem*. 2009; 233: 1395–1406p.
24. Campana FP, Buqa H, Novak P. *Electrochem Commun*. 2008; 10: 1590–1593p.

25. Hu C, Tao L, Yong Y. *Prog Chem*. 2006; 18: 542–549p.
26. Inaba M, Kawatate Y, Funabiki A. *Electrochim Acta*. 1999; 45: 99–105p.
27. Lee KT, Jeong S, Cho J. *Accounts Chem Res*. 2013; 46: 1161–1170p.
28. Morigaki K. *J Power Sources*. 2002; 104: 13–23p.
29. Zhang J, Yang XC, Wang R et al. *J Phys Chem C*. 2014; 118: 20756–20762p.
30. Zhang SS. *J Power Sources*. 2006; 162: 1379–1394p.
31. Xu K. *Chemical Reviews*. 2004; 104: 4303–4417p.
32. Cresce AV, Russell SM, Baker DR et al. *Nano Lett*. 2014; 14: 1405–1412p.
33. Zhang J, Wang R, Yang X. *Nano Lett*. 2012; 12: 2153–2157p.
34. Shin H, Park J, Han S et al. *J Power Sources*. 2015; 277: 169–179p.
35. Domi Y, Doi T, Yamanaka T et al. *J Electrochem Soc*. 2013; 160: A678–A683p.
36. Martin L, Martinez H, Ulldemolins M. *Solid State Ionics*. 2012; 215: 36–44p.
37. Martin L, Martinez H, Poinot D et al. *J Power Sources*. 2014; 248: 861–873p.
38. Lucas IT, Pollak E, Kostecki R. *Electrochem Commun*. 2009; 11: 2157–2160p.
39. Mandal B. *Solid State Ionics*. 2004; 175: 267–272p.
40. Li L, Zhou S, Han H, et al. *J. Electrochem. Soc*. 2011; 158: A74–A82p.
41. Liu XR, Wang L, Wan LJ et al. *ACS Applied Materials & Interfaces*. 2015; 7: 9573–9580p.
42. Mogi R, Inaba M, Iriyama Y. *Journal of Power Sources*. 2002; 108: 163–173p.
43. Chemelewski KR, Lee ES, Li W. *Chemistry of Materials*. 2013; 25: 2890–2897p.
44. Wang CC, Hsieh WP, Shiao MH. *Journal of the Electrochemical Society*. 2003; 150: B199–B204p.
45. Wang ZX, Sun YC, Chen LQ et al. *Journal of the Electrochemical Society*. 2004; 151: A914–A921p.
46. Wang ZX, Huang XJ, Chen LQ. *Journal of the Electrochemical Society*. 2004; 151: A1641–A1652p.
47. Lei JL, Li LJ, Kostecki R. et al. *Journal of the Electrochemical Society*. 2005; 152: A774–A777p.
48. Goonetilleke PC, Zheng JP, Roy D. *Journal of the Electrochemical Society*. 2009; 156: A709–A719p.
49. Menetrier M, Vaysse C, Croguennec L. *Electrochemical and Solid State Letters*. 2004; 7: A140–A143p.
50. Liu N, Li H, Wang ZX. *Electrochemical and Solid State Letters*. 2006; 9: A328–A331p.
51. Wursig A, Buqa H, Holzapfel M. *Electrochemical and Solid State Letters*. 2005; 8: A34–A37p.
52. Dupre N, Martin JF, Oliveri J et al. *Journal of the Electrochemical Society*. 2009; 156: C180–C185p.
53. He P, Zhang X, Wang YG et al. *Journal of the Electrochemical Society*. 2008; 155: A144–A150p.
54. Hirayama M, Sonoyama N, Ito M et al. *Journal of the Electrochemical Society*. 2007; 154: A1065–A1072p.
55. Rangappa D, Murukanahally KD, Tomai T. *Nano Lett*. 2012; 12: 1146–1151p.
56. CohenYS, Aurbach D. *Electrochem Commun*. 2004; 6: 536–542p.
57. Światowska-Mrowiecka J, Maurice V, Zanna S. *J Power Sources*. 2007; 170: 160–172p.
58. Fleutot B, Martinez H, Pecquenard B et al. *J Power Sources*. 2008; 180: 836– 844p.
59. Doi T, Inaba M, Tsuchiya H et al. *J Power Sources*. 2008; 180: 539–545p.

60. Liu RR, Deng X, Liu XR et al. *Chemical Communications*. 2014; 50: 15756 –15759p.
61. Yang S, Yan B, Li T et al. *Physical Chemistry Chemical Physics*. 2015; 17: 22235–22242p.
62. Seol D, Seo H, Jesse S et al. *Journal of Applied Physics*. 2015; 118: 072014p.
63. Jesse S, Kumar A, Arruda TM et al. *MRS Bulletin*. 2012; 37: 651–658p.
64. Zhu J, Lu L, Zeng K. *ACS NANO*. 2013; 7: 1666–1675p.
65. Balke N, Maksymovych P, Jesse S et al. *ACS NANO*. 2015; 9: 6484–6492p.
66. Arruda TM, Kumar A, Kalinin SV et al. *Nano Lett*. 2011; 11: 4161–4167p.
67. Jesse S, Balke N, Eliseev E et al. *ACS NANO*. 2011; 5: 9682–9695p.
68. Balke N, Jesse S, Morozovska AN et al. *Nature Nanotechnology*. 2010; 5: 749 –754p.
69. Arruda TM, Kumar A, Kalinin SV et al. *Nanotechnology*. 2012; 23.
70. Zhu X, Ong CS, Xu X et al. *Scientific Reports*. 2013; 3: 1084p.
71. Ding F, Xu W, Graff GL et al. *J Am Chem Soc*. 2013; 135: 4450–4456p.
72. Scrosati B. *Journal of Solid State Electrochemistry*. 2011; 15: 1623–1630p.
73. Yan K, Lee HW, Gao T et al. *Nano Lett*. 2014; 14: 6016–6022p.
74. Aurbach D, Cohen Y. *J Electrochem Soc*. 1996; 143: 3525–3532p.
75. Cohen YS, Cohen Y, Aurbach D. *Journal of Physical Chemistry B*. 2000; 104: 12282–12291p.
76. Mogi R, Inaba M, Abe T, et al. *J Power Sources*. 2001; 97(8): 265–268p.
77. Mogi R, Inaba M, Iriyama Y et al. *J Electrochem Soc*. 2002; 149: A385–A390p.
78. Beaulieu LY, Beattie SD, Hatchard TD et al. *J Electrochem Soc*. 2003; 150: A419–A424p.

Cite this Article
Shu-Wei Wang, Shi-Qiang Huang, Yan Jin *et al.* Application of atomic force microscopy for the study of lithium-ion batteries. *Journal of Nanoscience, Nanoengineering and Applications*. 2015; 5(3): 35–47p.